

Article

Numerical Simulation Analysis of Acoustic Emission Characteristics during the Drilling Pressure Relief Process in Coal Seams under Different Influencing Factors

Ji Ma ^{1,*}, Jiashuo Li ¹, Shuai Zhang ^{2,3}, Shengtao Yang ⁴, Xiaohang Dong ¹ and Dongsheng Liu ¹

¹ School of Safety Science and Engineering, Henan Polytechnic University, Jiaozuo 454003, China; lijiaoshuo990308@gmail.com (J.L.); jack666jack666jack666@outlook.com (X.D.); liu1426098061@163.com (D.L.)

² School of Civil Engineering, Beijing Jiaotong University, Beijing 100044, China; 9331@bjtu.edu.cn

³ Key Laboratory of Safety and Risk Management on Transport Infrastructures of Ministry of Transport, Beijing 100044, China

⁴ College of Construction Engineering, Jilin University, Changchun 130026, China; taoyang20@mails.jlu.edu.cn

* Correspondence: showsma@hpu.edu.cn

Abstract: Drilling pressure relief is a widely recognized and applied key technique to reduce the risk of rock burst occurrence, and its field-applied effects are also obvious. In this paper, the values of micro parameters required for discrete element method (DEM) simulations were first determined through indoor experiments and parameter calibration. Then, drilling pressure relief numerical simulations were conducted with different drilling diameters, drilling angles, and drilling depths. The results show that as the depth and diameter of the borehole increase, the peak strength of the coal sample first rapidly decreases, and then slowly decreases. The 30 mm depth and 14 mm diameter of the borehole are, respectively, the critical thresholds for the transition of the peak strength decrease rate; as the drilling angle increases, the peak strength of the coal sample first rapidly decreases and then increases, and the drilling angle of 25° is the critical threshold for the peak strength transformation. At the same time, the type of coal sample failure also changes from conjugate shear fracture to single slope shear fracture with the increase of three drilling parameters; shear and tensile cracks are the main types of micro fractures in coal samples. The research results are of great significance for improving the pressure relief plan of coal seam drilling and preventing and controlling rock burst disasters.

Keywords: rockburst; acoustic emission (AE); drilling pressure relief; moment tensor; discrete element method



Citation: Ma, J.; Li, J.; Zhang, S.; Yang, S.; Dong, X.; Liu, D. Numerical Simulation Analysis of Acoustic Emission Characteristics during the Drilling Pressure Relief Process in Coal Seams under Different Influencing Factors. *Processes* **2023**, *11*, 3277. <https://doi.org/10.3390/pr11123277>

Academic Editor: Jose Carlos Pinto

Received: 22 October 2023

Revised: 6 November 2023

Accepted: 16 November 2023

Published: 23 November 2023



Copyright: © 2023 by the authors. Licensee MDPI, Basel, Switzerland. This article is an open access article distributed under the terms and conditions of the Creative Commons Attribution (CC BY) license (<https://creativecommons.org/licenses/by/4.0/>).

1. Introduction

With the gradual deepening of coal resource mining, the geological environment and conditions in coal mines have become more complex, and the incidence and severity of coal and rock dynamic disasters such as rock bursts have significantly increased. It is extremely important to prevent and control coal and rock dynamic disasters in deep mines [1]. Drilling pressure relief is an effective method for preventing and controlling rock bursts [2,3]. It has been included in the criteria for rock bursts in China and is the first step to be carried out in the mining work of rock burst mines. For the study of controlling rock burst disasters through drilling pressure relief, the efficiency of drilling pressure relief is a key scientific issue of primary concern [4].

The essence of this key issue is to grasp the damage and deterioration characteristics of the surrounding rock mass during the process of drilling pressure relief, to formulate the optimal scheme for the physical parameter layout of drilling. Thus, a system of evaluation parameter indexes before and after the drilling pressure relief during the mining process of the working face can be developed. Therefore, scholars and experts in this field have

conducted a large amount of practical study and theoretical work, and have achieved a large number of related outcomes. The method of drilling pressure relief is considered the most convenient and efficient method in Europe and America, while in Germany, this method is the only measure approved by national departments [4,5]. In the last century, the former Soviet Union has also done a lot of work on the study of drilling pressure relief [6], and the influence of different drilling intervals and drilling diameters on the pressure relief effect was obtained through experimental research. Ortlepp and Stacey [7] analyzed the prevention and control mechanism of drilling pressure relief technology for rock burst disasters from the test results. Reyes and Einstein [8] carried out physical simulation tests of coal and rock mechanics. Refs. [9,10] conducted a systematic study on the influence of drilling shape on the mechanical properties and fracture characteristics of porous rocks under uniaxial loading. Refs. [11,12] studied the elastic energy dissipation, angle of stress transfer, and plastic behavior of large-diameter decompression drilling in coal seams under high stress conditions. A reasonable drilling pressure relief plan has been determined. Refs. [10,13] conducted uniaxial compression tests on drilled coal materials to study the changes in parameters such as strength and the energy dissipation index, and analyzed the crack propagation characteristics of rocks around the drilled holes in the experiments. Zhang et al. [12] found experimentally that variable diameter drilling can enhance the plasticity of the sample while weakening the brittleness, so that the impact tendency can be reduced. Zhang et al. [13] studied the shear failure characteristics caused by compressive stress concentration around non-circular drilling. Li et al. [14] investigated the energy, stress, and impact tendency of the pressure relief principle of drilling. The method of using electromagnetic wave CT detection technology to test the pressure relief effect of drilling was proposed and verified.

With the emergence of numerical simulation technology, the problem of the “black box” is transparent, and the study of the drilling pressure relief process can be realized. Refs. [15–17] used numerical simulation to study the pressure relief effect under different drilling intervals and diameters. Based on the theory of energy propagation attenuation, Refs. [17,18] found through numerical simulation of rock samples with different borehole diameters that an increase in borehole diameter can lead to better pressure relief effects in the borehole. Refs. [19,20] used numerical simulation software to model the process of drilling and unloading pressure in rock burst tunnels, and compared and analyzed the stress field of the surrounding rock with and without unloading pressure. Pressure relief is achieved by the energy accumulated in the high stress zone after drilling, which causes the rock mass between the boreholes to be damaged. Refs. [18,21] used numerical simulation software to simulate the stress concentration zone in the excavation direction of deep coal tunnels, and obtained the pressure relief effects of directional drilling, roof stratification, and axial force changes of anchor rods. Wen et al. [20] studied the number and the propagation law of fractures for coal samples in the process of drilling pressure relief under different parameter conditions by numerical simulation software. However, there are few reports on the microscopic mechanism of pressure relief by drilling in coal seams, and studies on the pressure relief scheme of drilling under the influence of different physical factors are also extremely rare.

Based on the above, this paper focuses on the macroscopic and microscopic mechanical properties and the optimal physical parameters of drilling in the process of pressure relief in coal seams. This study is based on the Hulusu Coal Mine located in Ordos City, Inner Mongolia Autonomous Region, China, with engineering technology as the background. Experimental and numerical simulation studies on the pressure relief of drilling in coal seams under the influence of different physical factors were carried out. The findings of the study can be beneficial for the revelation of the microscopic mechanism and the proposal of the optimization scheme of the pressure relief in coal seams. In this article, a combination of indoor tests and numerical simulations was used to study the failure mode and acoustic emission characteristics of borehole pressure relief in coal seams. These findings from

the current work can provide data support for the practical application and promotion of borehole pressure relief technology.

2. Engineering Overview and Pressure Relief Mechanism of Drilling

Introduction to the Hulusu Coal Mine (the research object of the current study): in recent years, dynamic disaster accidents have occurred frequently in mines in Shaanxi and Inner Mongolia. For example, on 18 November 2017, there was a strong dynamic force in the return airway of the 21,103 working face of Hulusu Coal Mine in Huijierte Mining Area, which caused a side heave of the coal pillar instantaneously, with a maximum displacement of 0.7 m. The safety exit of the tail section of the working face was blocked, and 10 single bodies were bent instantaneously. Subsequently, on 6 February 2018, the 21,103 working face was advanced by 85–133 m. The large-scale floor heave, drum side, and coal pillar side of the return air roadway were broken, 10 single pillars of coal pillar side were thrown to the solid side, 17 wooden stacks were overturned, and coal body burst from the floor.

As shown in Figure 1, the Hulusu Mine belongs to the Huijierte Mining Area. The entire mining area is located in Ordos, Inner Mongolia Autonomous Region, and is under the jurisdiction of Tuke Town, Wushen Banner and Taige Sumu, Yijinhuluo Banner. The east–west tilt width of the Hulusu Mine is 13.0 km, the north–south length is 7.4 km, and the total area is about 92.76 km². The production progress of Hulusu Mine is in the recovery of a 2-1 coal seam. The overall trend of the coal seam is northeast, and it is inclined to the northwest; the formation dip angle is 1~4°. The depth of the 2-1 coal seam is more than 600 m, and its roof lithology is mainly siltstone and sandy mudstone, followed by medium and fine sandstone. The floor lithology is mainly siltstone and sandy mudstone. According to the ‘Hulusu Coal Mine 2-1 Coal Rock Burst Tendency Identification Report’, the 2-1 coal seam has a strong burst tendency, and the roof and floor have a weak burst tendency. The second panel is located in the central west of the Hulusu Mine. On the north side of the area, there are three main roadways of the 2-1 coal seam, covered with Quaternary aeolian sand, with less vegetation in the area. It is a desert and semidesert area, and its surface is a plateau-accumulated hilly landform. The ground elevation of the second panel is +1304.50~+1341.20 m, the underground elevation is +655~+680 m, and the buried depth is 624~685 m.

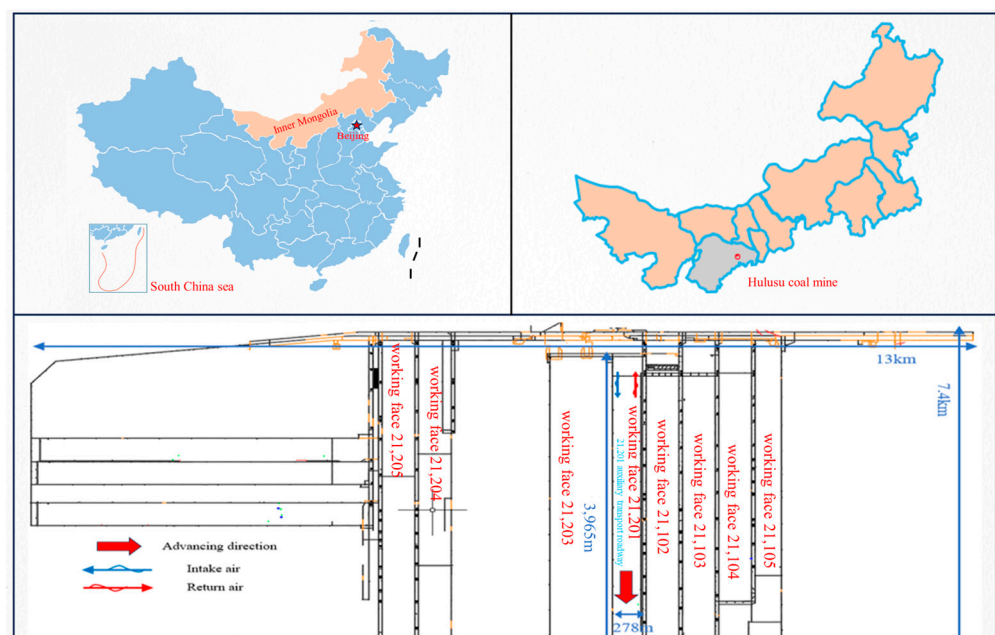


Figure 1. Schematic diagram of the location of Hulusu Coal Mine.

The 21,201 working face is located in the eastern part of the second panel. During the initial mining period, the surface width was 293 m. Mining work is 480 m, the surface width is 278 m, and the advancing length is 3965 m. Due to hidden factors such as the rock burst tendency of coal-rock, erosion zones, faults, goaf field and folds, a comprehensive evaluation has shown that there is a risk of a rock burst disaster during the mining of the 21,201 working face.

As a classic rock burst prevention and control method, the principle of drilling pressure relief is to reduce the stress concentration in the target area by drilling in the coal seam, or to change the mechanical properties of the coal within the target area so that the stable and controllable failure process of the coal can replace the unstable failures of the coal that may occur, which can effectively eliminate or reduce the risk of deformation and instability of the surrounding rock of the roadway. As shown in Figure 2b, when drilling is carried out in high-stress coal seams, cracks and ruptures occur in the coal near the borehole under the action of stress, resulting in a crushing zone of the coal near the borehole that is much larger than the diameters of the borehole. After multiple drills, these crushing zones can intersect with each other and generate a large-scale pressure relief zone in the entire coal seam, thereby effectively reducing the peak value of stress concentration and transferring the stress concentration zone to the deep area, as in Figure 2c. On the one hand, the fracture zone formed by drilling reduces the stress concentration of the coal seam, thus greatly reducing the impact risk and playing a role in pressure relief; on the other hand, drilling also changes the mechanical properties of coal seams and weakens the ability of coal seams to store elastic energy, thus reducing the risk of rock burst disasters. The pressure relief principle of drilling in coal is shown in Figure 2a.

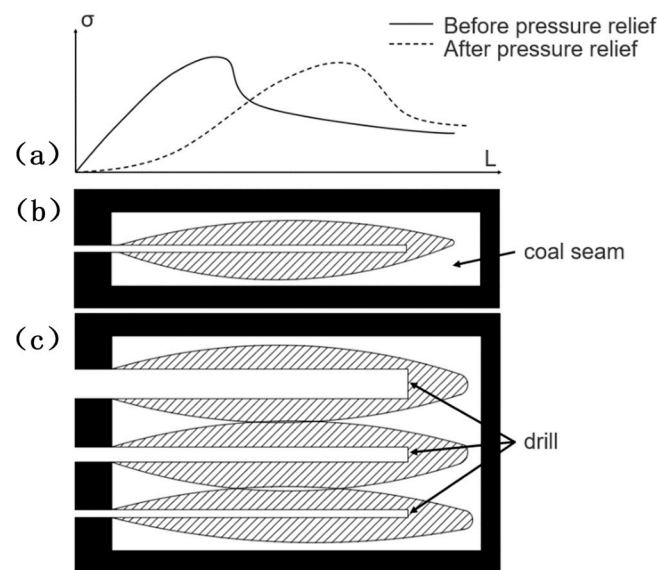


Figure 2. Schematic of coal seam drilling relief [22]. (a) Stress changes before and after pressure relief; (b) The influence range of single borehole pressure relief; (c) The influence range of pressure relief of multiple boreholes with different diameters.

3. Numerical Model Diagram and Sample

3.1. Basic Concept

The DEM model of coal samples in this paper is modeled by the PFC numerical simulation software, including the particles and contact between particles, as shown in Figure 3. The particles of the coal specimen were modeled as rigid spheres with a certain range of particle sizes. The contacts between the coal particles were chosen through the parallel bond model [21]. As a mechanical interaction law between particles in PFC software Version 6.0, the principle of this law is equivalent to establishing two sets of microscopic vertical spring units between two particles, including springs perpendicular to the contact

surface (normal springs) and springs parallel to the contact surface (tangential springs). Through the action of force, the maximum tensile and shear stresses generated between the two particles on the parallel bond are as follows [23,24]:

$$\bar{\sigma}_{\max} = \frac{-\bar{F}_n}{A} + \frac{|\bar{M}_s|\bar{R}}{I} < \bar{\sigma} \tag{1}$$

$$\bar{\tau}_{\max} = \frac{-\bar{F}_s}{A} + \frac{|\bar{M}_n|\bar{R}}{J} < \bar{\tau} \tag{2}$$

where \bar{F}_n is the normal force, \bar{F}_s is the tangential force; \bar{M}_n is the bending moment, and \bar{M}_s is the torque; J, A, I are the polar moment of inertia, the contact area, and the moment of inertia.

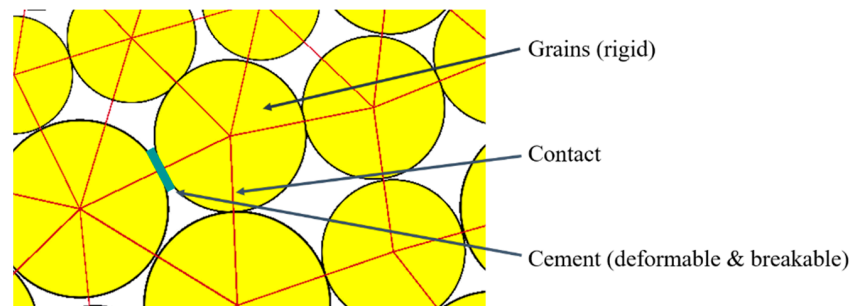


Figure 3. Bonded-particle model [23].

For the parallel bond contact model, the microscopic parameters mainly used to describe the physical properties are: normal strength $\bar{\sigma}$ and tangential strength $\bar{\tau}$, particle normal stiffness k_n and tangential stiffness k_s , bonding normal stiffness \bar{k}_n and bonding tangential stiffness \bar{k}_s friction coefficient. When the shear stress on the contact exceeds the shear strength, the micro-spring between the particles is tangentially destroyed, the shear strength of the contact between the particles is reduced to the residual strength, and the normal force and friction factors affect the residual strength. When the tensile stress on the contact exceeds the tensile strength, the micro-spring between the particles breaks and tensile cracks appear, and the contact between the particles loses the tensile strength, as shown in Figure 4 [22].

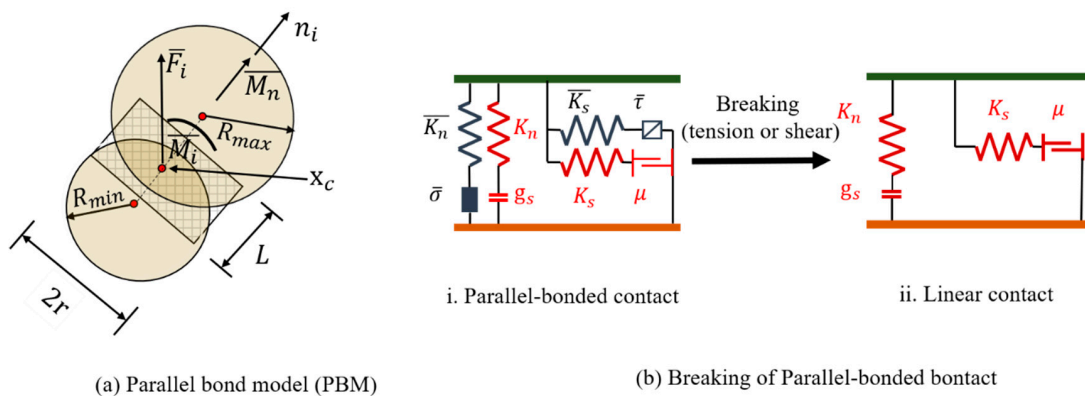


Figure 4. Parallel bond model and bond breaking [23].

Here is a description of the contact method (primarily the change of force and moment updated as the timestep) in the parallel bond contact model. The contact force is resolved into linear force F^l , dashpot force F^d , and the parallel-bond force \bar{F} . The contact moment M_c is the parallel-bond moment \bar{M} , which can be resolved into torsional moment \bar{M}_t and bending moment \bar{M}_b .

For the force group, including linear force F^l , dashpot force F^d and parallel-bond force \bar{F} can be resolved into a normal component and shear component. These three forces can be updated as follows:

For the linear force F^l :

$$F_n^l = k_n \times \Delta g_n \text{ (normal)}; F_s^l = k_s \times \Delta g_s \text{ (shear)}$$

where k is the stiffness and Δg is the variational quantity in distance of ball–ball or ball–wall.

For the dashpot force F^d :

$$F_n^d = (2\beta_n \sqrt{m_c k_n}) \times \dot{\delta}_n \text{ (normal)}; F_s^d = (2\beta_s \sqrt{m_c k_s}) \times \dot{\delta}_s \text{ (shear)}; m_c = \frac{m_1 m_2}{m_1 + m_2}$$

where m_1 and m_2 are the mass of contact balls, β is the damping ratio, $\dot{\delta}$ is the relative translational velocity of ball–ball or ball–wall.

For the parallel-bond force \bar{F} :

$$\bar{F}_n = -(\bar{F}_n)_0 + \bar{k}_n \bar{A} \Delta \delta_n \text{ (normal)}; \bar{F}_s = -(\bar{F}_s)_0 + \bar{k}_s \bar{A} \Delta \delta_s \text{ (shear)}$$

where $(\bar{F})_0$ is the parallel component force at the beginning of the time step, \bar{A} is the area of the bond, \bar{k} is the stiffness, and $\Delta \delta$ is the relative normal displacement increment.

For the moment group, the parallel-bond moment \bar{M} can be resolved into a torsional component and bending group.

The torsional moment is updated:

$$\bar{M}_t = -(\bar{M}_t)_0 + \bar{k}_s \bar{J} \Delta \theta_t,$$

where $(\bar{M}_t)_0$ is the twisting moment at the beginning of the time step, \bar{J} is the polar moment of inertia of the bond, and $\Delta \theta_s$ is the relative twist rotation.

The bending moment is updated:

$$\bar{M}_b = -(\bar{M}_b)_0 + \bar{k}_n \bar{I} \Delta \theta_b,$$

where $(\bar{M}_b)_0$ is the bending moment at the beginning of the time step, \bar{I} is the moment of inertia of the bond, and $\Delta \theta_b$ is the bend–rotation increment.

3.2. AE Simulation Method Based on Moment Tensor

This section presents a moment tensor-based acoustic emission simulation method. It is assumed that the AE event is composed of a bond rupture event in a specified space–time range. The derivation [25] is as follows:

According to the variation of the contact force of the particles in the fracture zone, the moment tensor is obtained [26,27]:

$$M_{ij} = \sum_S \Delta F_i R_j \quad (3)$$

where ΔF_i is the i direction component of the change value of the contact force and R_j is the j direction component of the distance between the contact point and the event center. S is the path enclosed by all contacts of the source particles (bonded broken particles).

The moment tensor with the maximum scalar moment value is used as the moment tensor of each AE event and stored. The expression of the scalar moment is [28]:

$$M_0 = \left(\sum_{j=1}^3 m_j^2 / 2 \right)^{1/2} \quad (4)$$

where m_j is the No. j eigenvalue of the moment tensor matrix.

The rupture strength of acoustic emission events can be calculated by the following formula [29]:

$$M_w = \frac{2}{3} \lg M_0 - 6 \quad (5)$$

After the shear fracture occurs, the time for the generated wave to be transmitted to the crack boundary is twice the duration of the micro-crack. During this period, the value of the moment tensor is recalculated and updated at each step. If no new micro-cracks appear during this period, it is considered that there is only one micro-crack in this AE event; if a new micro-crack is generated during this period, and the influence range of the new and old cracks is staggered, the micro-crack is attributed to the same AE event, that is, multiple micro-cracks appear in this AE event, and the calculation and extension of the duration of the micro-crack are updated.

Wang et al. [30] proposed to characterize the rupture type of AE events by the isotropic and anisotropic components of the moment tensor, namely:

$$R = \frac{tr(M) \times 100}{|tr(M)| + \sum |m_i^*|} \quad (6)$$

$$tr(M) = m_1 + m_2 + m_3 \quad (7)$$

$$m_i^* = m_i - tr(M)/3 \quad (8)$$

where $tr(M)$ is the trace of a tensor; m_i is the eigenvalue of the tensor; and m_i^* is the eigenvalue partial tensor.

The specific criteria are as follows: $R > 30\%$, tensile failure; $-30\% \leq R \leq 30\%$, shear failure; and $R < -30\%$, mixed failure.

Because there is an exponential relationship between the amplitude of the acoustic emission event M and its value N , the relationship is described by the Gutenberg–Richter formula [31]:

$$\lg N = a - bM \quad (9)$$

where N is the number of AE events with a moment tensor amplitude greater than M . For the slope b when the proportion of signal components with large energy is large, the b value is small; when the proportion of signal components with large energy is small, the b value is larger.

3.3. Sample Preparation and Parameter Calibration

The calibration of microscopic parameters is the primary matter in the application of DEM software 6.0 to simulate coal and rock problems. The microscopic parameters involved in DEM software can not be obtained by tests. Therefore, it is necessary to continuously verify the macroscopic data such as the Poisson ratio, uniaxial compressive strength, and elastic modulus obtained by tests. Based on the experience of predecessors and their own experience, the microscopic parameters are repeatedly adjusted by the trial and error method to calibrate, so that the overall parameters of the numerical model are in line with the actual results. Firstly, an indoor uniaxial compression test is needed to obtain the macroscopic mechanical parameters of the coal.

The experimental coal sample was taken from Hulusu Coal Mine. In order to be more in line with the actual situation of the site, the original bulk coal sample was directly drilled in the coal mine, and the sample was cut into $100 \times 100 \times 100$ (mm) standard cubes. The standard cube samples were three groups. The specific size and shape are shown in Figure 5. The RMT-150B (Institute of Rock and Soil Mechanics, Chinese Academy of Sciences, Wuhan, China) rock mechanics test system was used in the experiment. The axial load was measured by a 1000 kN force sensor with a load accuracy of 1.0×10^{-3} kN. The axial compression deformation was measured by a 5.0 mm displacement sensor. The circumferential deformation was measured by two 2.5 mm displacement sensors with a

deformation accuracy of 1.0×10^{-3} mm. The stress–strain curve obtained by the experiment is shown in Figure 6.

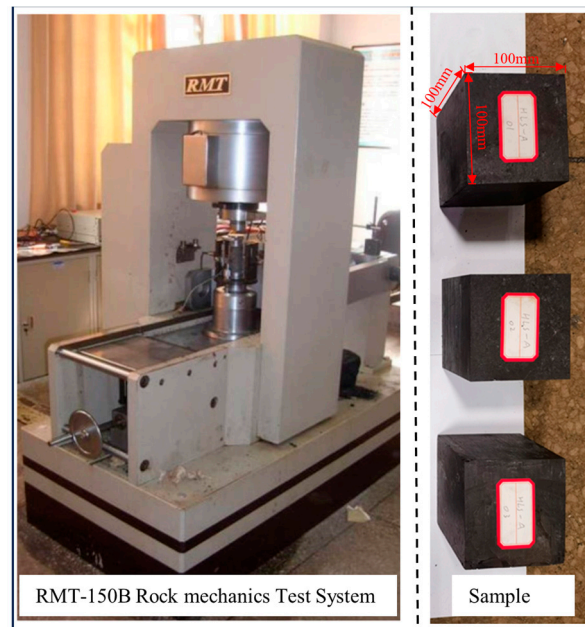


Figure 5. RMT-150B rock mechanics testing system (left) and experimental specimens (right).

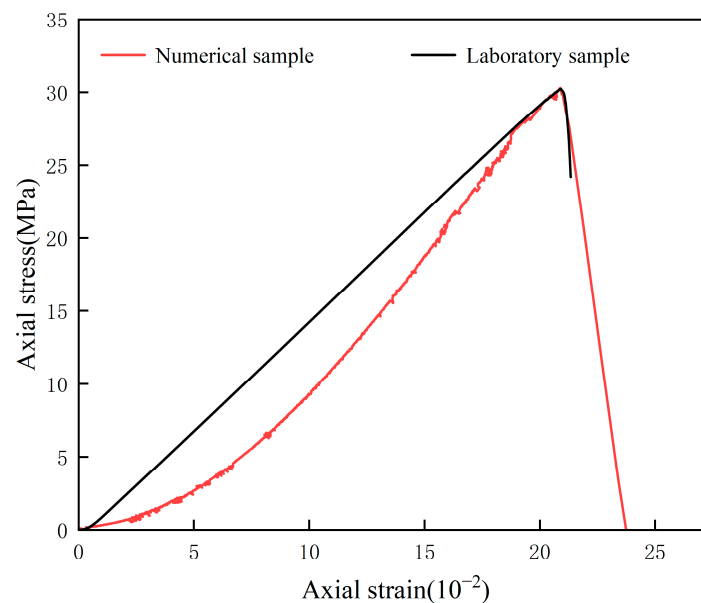


Figure 6. The contrast of stress–strain curves between numerical simulations and laboratory tests.

A rock sample with diameters of $\Phi 100 \text{ mm} \times 100 \text{ mm} \times 100 \text{ mm}$ was established. For the rock particles, a normal distribution was used for a particle radius range from 1.5 to 1.7 mm. A range of maximum and minimum particle radii with small differences ensured a more homogeneous generation of rock samples. Rock particles with a density of 2700 kg/m^3 and an elastic modulus of 0.775 GPa were adopted to be close to the characteristics of the actual sample. The contact model between the rock particles adopted parallel bonding contact. The parameters of the parallel bonding contact are listed in Table 1. It was confirmed from numerous pre-tests that the peak value and rise ascent of simulated stress were significantly affected by the friction coefficient and effective modulus of rock particles, respectively. For this experience, the parameters shown in Table 1 were regulated by continuously modifying until the stress–strain characteristics of the numerical

simulation matched the experiments. From Figure 6, it can be seen that the simulated values are very close to the measured values, indicating that the microscopic parameters can accurately simulate the mechanical properties of coal. The proposed DEM parameters are shown in Table 1, which can better capture the mechanical behavior of the rock sample in this study. The effective modulus of the linear group and parallel bond group are all equal to 0.87×10^9 Pa. The friction coefficient and normal to shear stiffness ratio are equal to 0.1 and 1.5, respectively. In addition, the tensile strength and cohesion of the contact are equal to 2.2137×10^7 and 8.1989×10^6 , respectively.

Table 1. Micromechanical parameters of the DEM model.

BPM Properties	Parameter	Value
Grain	Density (kg/m ³)	2700
	R _{min} (mm)	0.0015
	R _{max} (mm)	0.0017
Contact	Elastic modulus (GPa)	0.775
	Effective modulus of the linear group (Pa)	0.87×10^9
	Effective modulus of the parallel bond group (Pa)	0.87×10^9
	Normal to shear stiffness ratio	1.5
	Tensile strength of the parallel bond group (Pa)	2.2137×10^7
	Cohesion of the parallel bond group (Pa)	8.1989×10^6
	Friction coefficient	0.1

In this section, the influence of different drilling diameters and depths on the strength of the test block and the form of surrounding crack propagation were studied by means of laboratory tests and DEM simulation, so as to understand the mechanism of drilling pressure relief more comprehensively.

4. Drilling Pressure Relief Test Scheme and Model Establishment

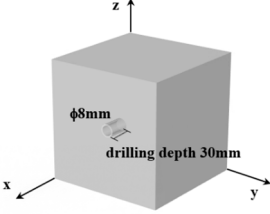
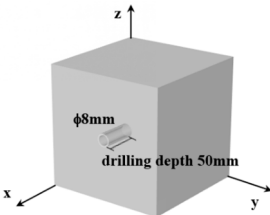
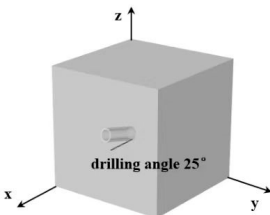
The influence of drilling depths, drilling diameters, and drilling angles on the effect of drilling pressure relief cannot be ignored. This experiment attempted to study the AE characteristics and physical influencing factors of different drilling depths, drilling diameters, and drilling angles in the process of drilling pressure relief. The influence of different parameters on the strength and AE characteristics of the sample under uniaxial compression was compared and analyzed. The specific experimental scheme is shown in Table 2.

In this section, a standard cube numerical model of $100 \times 100 \times 100$ (mm) has been established, and the microscopic parameters have been calibrated according to the results of the uniaxial loading compression tests. The numerical model is consistent with the macroscopic parameters of indoor experiment coal samples.

The dynamic excavation unloading process experiment of the numerical model under uniaxial loading conditions is shown in Figure 7. Initially, numerical specimens were prepared in the area surrounded by the walls (as shown in Figure 7a). To subject the numerical specimens to the pressure equivalent to the field specimens buried in the subsurface at an appropriate location, a confining pressure setting of 40 kPa in all directions was performed for the numerical specimens. In other words, a more compact rock sample was generated after the process of confining the specimen in all directions. Once the specimen with a specified strength was generated, the lateral walls were deleted and the activity of the rock sample in the lateral direction was no longer restricted. Then, a borehole was drilled, located in the middle of the front after the removal of the lateral walls. Finally, the uniaxial monotonic compressive testing using the axial displacement control method was carried out, and the loading rate was set to 0.005 mm/s. The loading method was as follows: The experimental loading rate was 0.005 mm/s, loading to 50% of the uniaxial peak strength, stopping loading to keep the deformation unchanged, drilling, keeping the deformation unchanged for 5 min, and then loading until the sample was destroyed. The dynamic

drilling unloading experiment was carried out on the numerical model following the above procedure.

Table 2. Experimental plan design.

Serial Number	Protocol	Parameter	Conceptual Drawing (Example)
I	Different drilling diameters	6, 8, 12, 14, 18, 20 mm	
II	Different drilling depths	10, 30, 50, 70, 90, 100 mm	
III	Different drilling angles	5, 15, 25, 35, 45°	

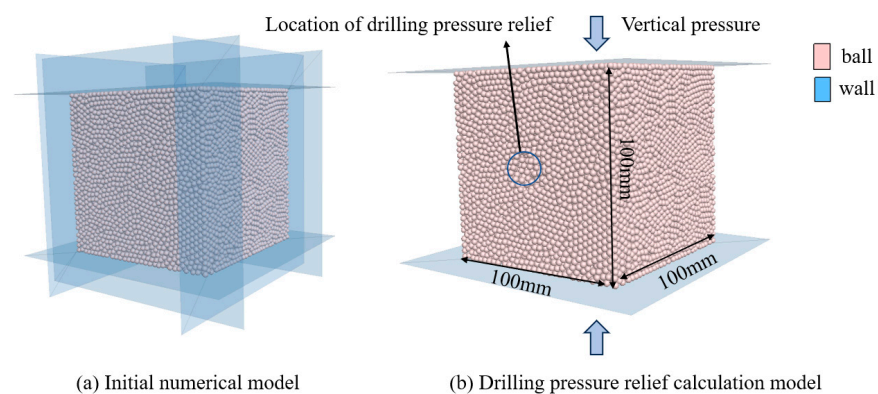


Figure 7. Pressure relief model for drilling.

5. Numerical Calculation Results

5.1. Strength Analysis of Samples under the Influence of Different Physical Factors

Figures 8 and 9 show the stress–strain curve of the sample under different drilling depths (the drilling radius was 8 mm). It can be seen from Figure 9 that the peak strength of the undrilled sample reached 30.23 MPa. After drilling at different depths, the peak strength of the sample decreased rapidly with the increase of the drilling depths (the drilling depths were 10 and 30 mm, respectively), then increased slowly (the drilling depths were 50 and 70 mm, respectively), and finally decreased slowly (the drilling depths were 90 and 100 mm, respectively). When the drilling depth was close to the central position of the sample, the influence scope ranges of the unloading zone were slightly weakened, indicating that the intersection of the lateral drilling unloading stress axis and the axial loading stress axis promoted the increase of sample strength. The peak strength of the sample with a

drilling depth of 30 mm was 17.2% lower than that of the sample without drilling, and the peak strength of the sample with a drilling depth of 100 mm was 6.88% lower than that of the sample with a drilling depth of 70 mm. Based on the above description, it can be seen that under uniaxial compression conditions, with the increase of drilling depths, when the drilling depth was below 30 mm, the pressure relief effect was the best.

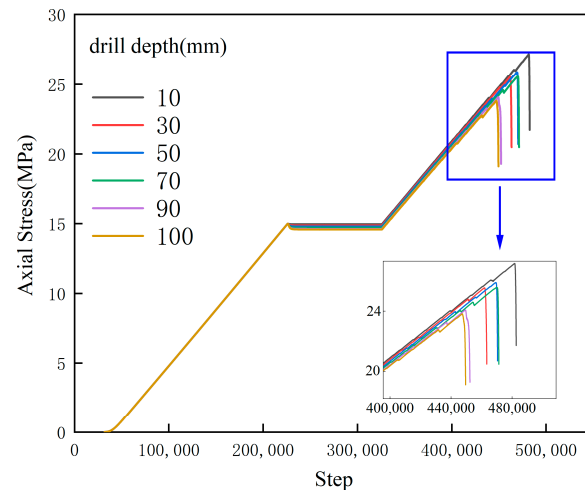


Figure 8. Stress–strain curve of samples under different drilling depths.

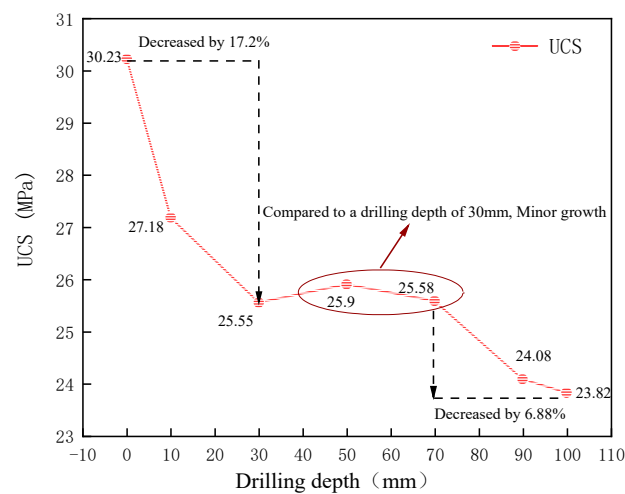


Figure 9. Curve of peak strength variation of samples under the influence of drilling depths.

Figures 10 and 11 are the stress–strain curves of the sample under different drilling diameters (the drilling depth was 30 mm). It can be seen from Figure 11 that the peak strength of the undrilled sample reached 30.23 MPa. After drilling with different diameters, the peak strength of the sample decreased with the increase of the borehole diameters (the drilling diameters were 6, 8, 12, 14, 18, and 20 mm, respectively) to 26.4, 26.0, 24.1, 23.23, and 23.01 MPa, respectively. It can be clearly seen that the strength of the sample decreased significantly with the increase of the drilling diameters. At the same time, it can be noted that the peak strength of the sample decreased rapidly with the increase of the diameters of the drilling (the depths of the drilling were 6, 8, 12, and 14 mm, respectively), and then decreased slowly (the depths of the drilling were 18 and 20 mm, respectively). The increase of the volume range of the borehole pressure relief area exacerbated the overall strength reduction of the sample. Based on the above description, it can be seen that under uniaxial loading, with other conditions unchanged, and with the increase of drilling diameters, the pressure relief effect of drilling increased with the increase of drilling diameters. The drilling diameter of 14 mm was the critical threshold. When the drilling diameter was

higher than this value, although the pressure relief effect of the drilling gradually increased, the effect gradually slowed down.

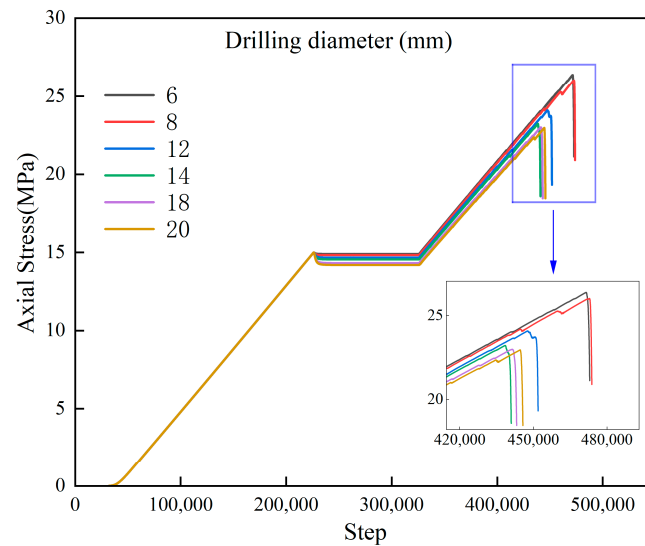


Figure 10. Stress–strain curve of samples under different drilling diameters.

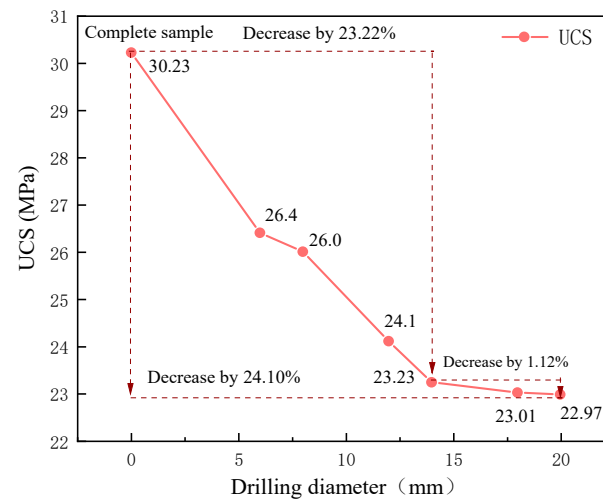


Figure 11. Curve of peak strength variation of samples under the influence of drilling diameters.

Figures 12 and 13 are the stress–strain curves of the sample under different drilling angles. The peak strength of the undrilled sample reached 30.23 MPa. After drilling with different angles, the peak strength of the sample decreased with the increase of the drilling angles (the drilling angles were 5°, 15°, and 25°, respectively) to 25.27 MPa, 25.08 MPa, and 24.31 MPa, which had a significant downward trend. Then, the peak strength of the sample increased with the increase of the drilling angles (the drilling angles were 35° and 45°, respectively) to 24.44 MPa and 24.73 MPa, and the upward trend was also obvious. The volume range of the unloading zone increased from the beginning to gradually decrease with the increase of the angle, and the overall strength weakening also showed a trend of first decreasing and then increasing with the change of the unloading zone range. The peak strength of the sample with a drilling angle of 25° was 3.8% lower than that of the 5° sample, while the peak strength of the sample with a drilling angle of 45° was 1.7% higher than that of the 25° sample. Based on the above analysis, it can be seen that under uniaxial loading, with other conditions unchanged, and with the increase of drilling angles, the pressure relief effect of drilling increased first and then decreased with the increase of drilling angles. The drilling angle of 25° was the critical threshold. When the drilling angle

exceeded 25° , the pressure relief effect of drilling gradually decreased. In summary, the pressure relief effect was best when the drilling angle was about 25° .

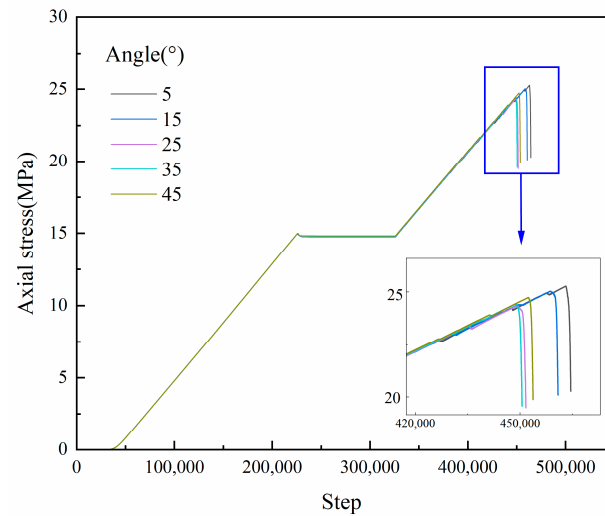


Figure 12. Stress–strain curve of samples under different drilling angles.

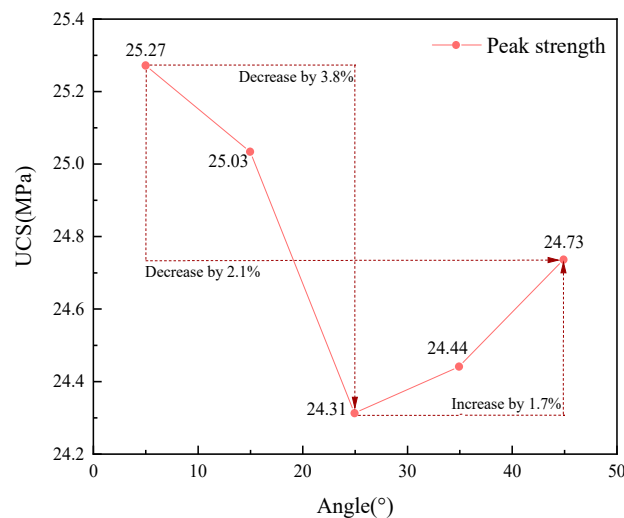


Figure 13. Curve of peak strength variation of samples under the influence of drilling angles.

5.2. Failure Mode Analysis of Samples under the Influence of Different Parameters

Figures 14–16 are the force chain contact diagrams of the samples under different drilling depths, different drilling diameters, and different drilling angles. From the three figures, it can be seen that the position of the failure crack and the distribution of the force chain in the surrounding area are more evacuated. The color of the force chain is deeper and the size of the force chain is smaller, which proves that this area had a better pressure relief effect. It can be seen from Figure 14 that when the drilling depth was 10–70 mm, the sample had a large pressure relief area. When the drilling depth was 90–100 mm, the pressure relief area of the sample was small, and when the drilling depth was 30 mm, the pressure relief area was the largest and the pressure relief effect was the best. It can be seen from Figure 15 that the sample had a large pressure relief area under different drilling diameters. When the borehole diameter was 14 mm, the pressure relief area was relatively large, the pressure relief effect was better, and the force chain distribution was more symmetrical. It can be seen from Figure 16 that the sample had a large pressure relief area under different drilling diameters, and the pressure relief area of the sample was relatively large when the drilling angle was 25° , and the pressure relief effect was better.

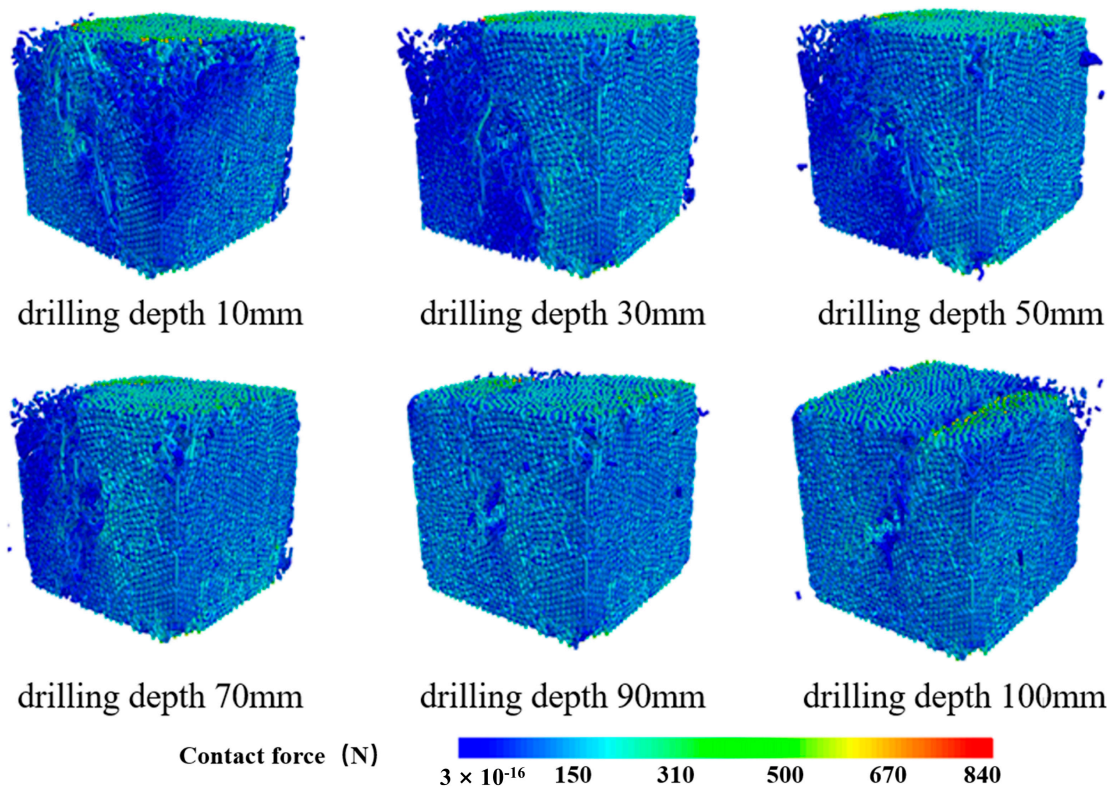


Figure 14. Contact diagram of force chains with different drilling depths.

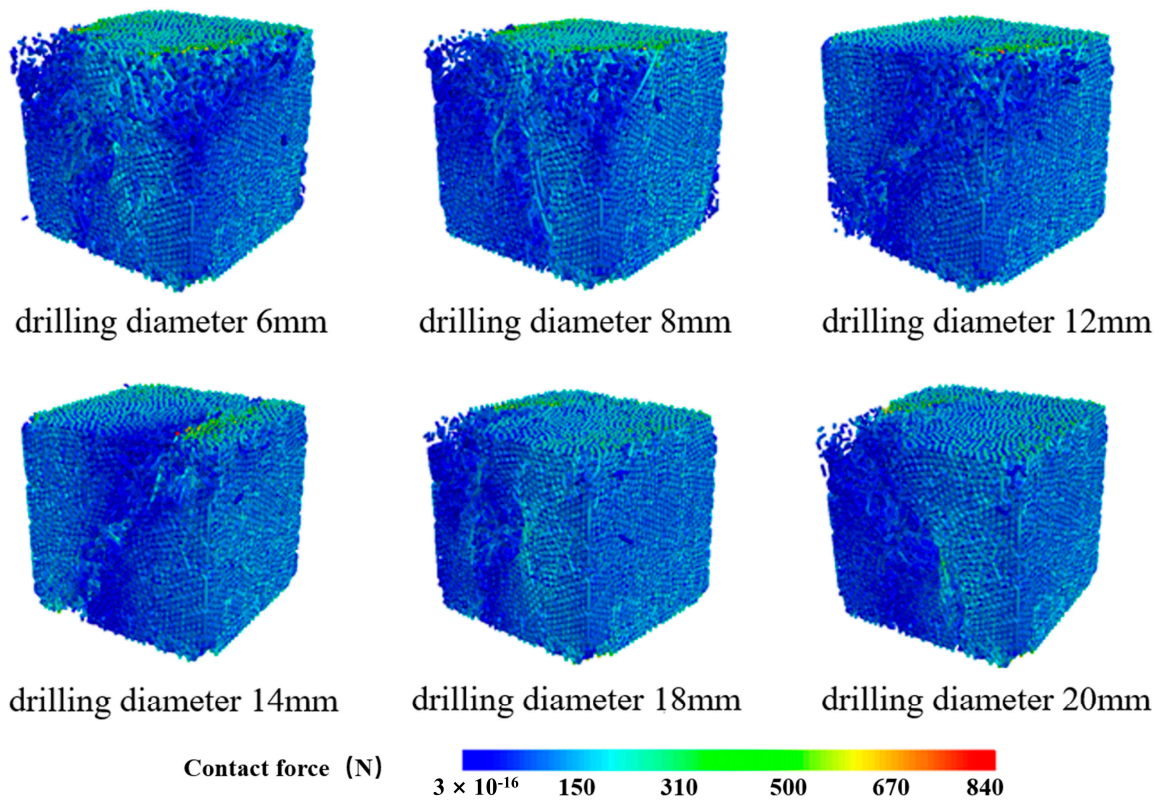


Figure 15. Contact diagram of force chains with different drilling diameters.

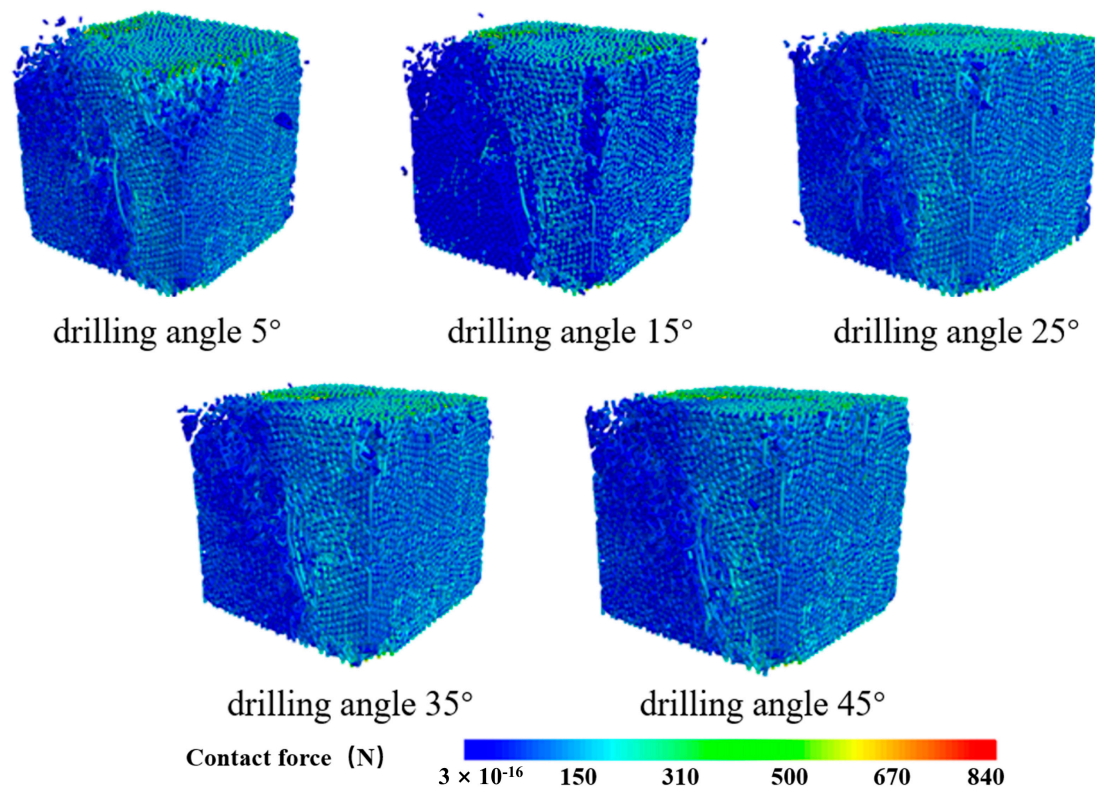


Figure 16. Contact diagram of force chains with different drilling angles.

Figure 17 shows the spatial distribution of the source and crack of the sample under different drilling depths. It can be seen from the diagram that the spatial distribution of the source and the spatial distribution of the crack had a high coincidence. This is because the crack generation process was accompanied by internal damage and vibration, so the area on the specimen surface where the macro-crack was generated had a large number and dense source distribution. When the drilling depth of the sample was 10 mm, the crack appeared as a conjugate shear fracture. As the drilling depth increased to 30 mm, the crack appeared as a single inclined plane shear fracture extending from the upper left corner to the lower right corner. From the drilling depth of 70 mm, the crack was still a single slope shear fracture, but its direction had changed from the upper right to the lower left. The critical value of drilling depths from the conjugate shear fracture to the single inclined plane shear fracture was 30 mm, which is consistent with the critical value of drilling depths when the optimal pressure relief effect is taken above.

Figure 18 shows the spatial distribution of the source and crack of the sample under different drilling diameters (the drilling depth was X mm, and the drilling angles was X°). It can be seen from the figure that the spatial distribution of the source and the spatial distribution of the crack also had a high coincidence. When the drilling diameter of the sample was 6–12 mm, the crack was characterized by a conjugate shear fracture. When the drilling diameter was 14 mm, the crack appeared as a single inclined plane shear fracture extending from the upper right corner to the lower left corner. From the drilling diameter to 18 mm, the direction of the shear fracture of the single inclined plane changed, and the trend of extending from the upper left to the lower right appeared. The critical value of drilling diameters from the conjugate shear fracture to the single inclined plane shear fracture was 14 mm, which is consistent with the critical value of drilling diameters when the optimal pressure relief effect is taken above.

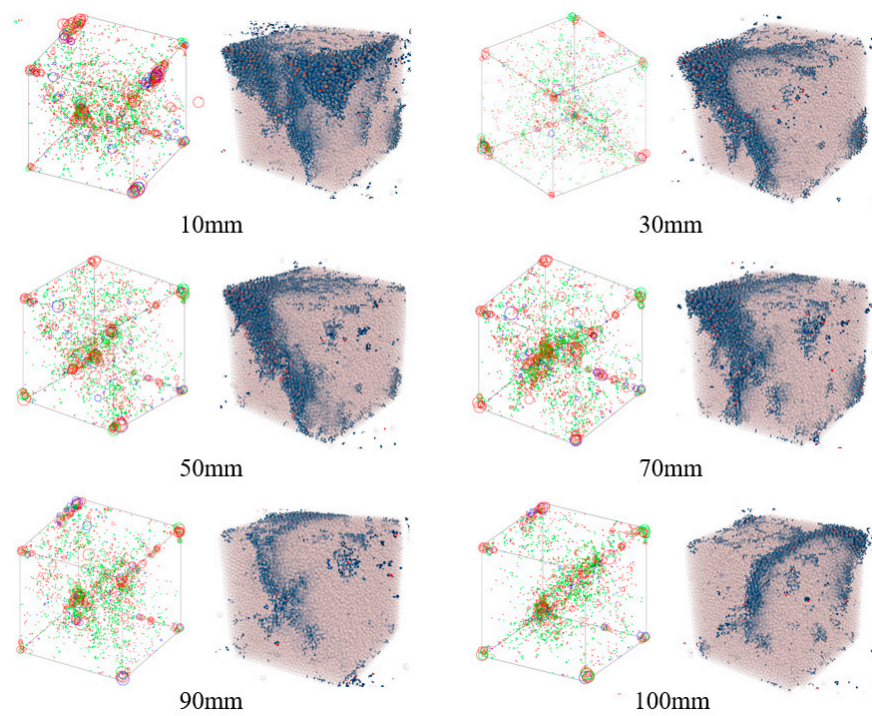


Figure 17. Spatial distribution of cracks and seismic sources under different drilling depths. Circles represent the location of seismic sources, where red indicates the deviatoric source; blue indicates the implosive source; green indicates the explosive source; and the size of the circle indicates the intensity of the seismic source.

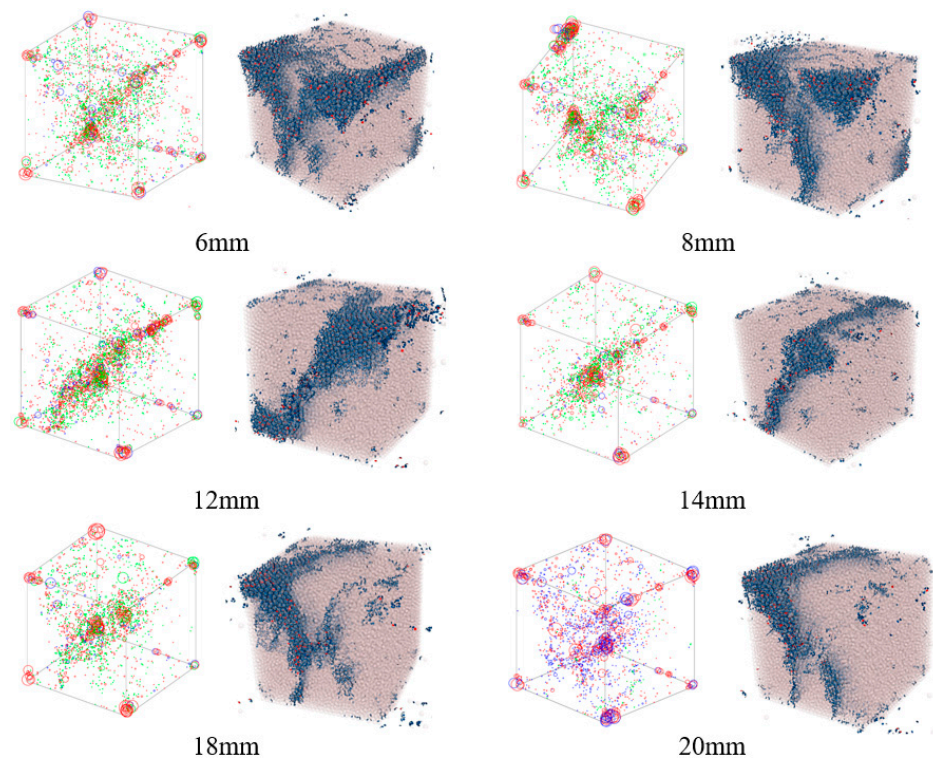


Figure 18. Spatial distribution of cracks and seismic sources under different drilling diameters. Circles represent the location of seismic sources, where red indicates the deviatoric source; blue indicates the implosive source; green indicates the explosive source; and the size of the circle indicates the intensity of the seismic source.

Figure 19 is the spatial distribution map of the source and crack of the sample under different drilling angles. It can be seen from the figure that the spatial distribution of the source and the spatial distribution of the crack also had a high coincidence. When the drilling angles were 5° and 15° , the crack appeared as a conjugate shear fracture. When the drilling angle was 25° , the crack appeared as a single inclined plane shear fracture extending from the upper left corner to the lower right corner. From the drilling angle to 35° , the direction of the shear fracture of the single inclined plane changed, and the trend of extending from the upper right to the lower left appeared. The critical value of drilling depths from the conjugate shear fracture to the single inclined plane shear fracture was 25° , which is consistent with the critical value of drilling angles when the better pressure relief effect is taken above.

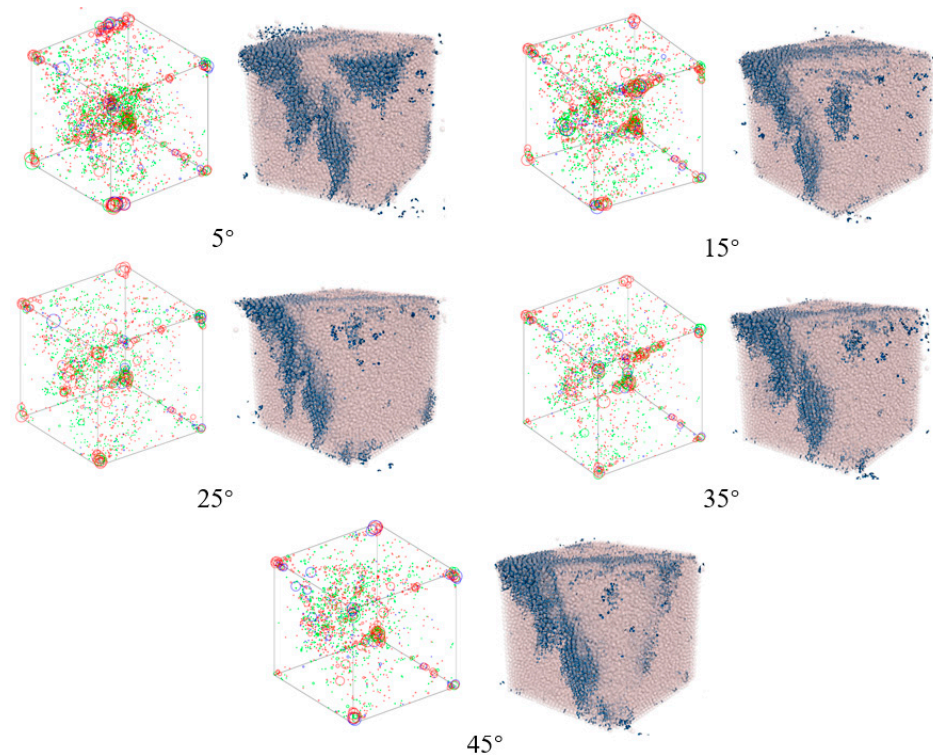


Figure 19. Spatial distribution of cracks and seismic sources under different drilling angles. Circles represent the location of seismic sources, where red indicates the deviatoric source; blue indicates the implosive source; green indicates the explosive source; and the size of the circle indicates the intensity of the seismic source.

5.3. Analysis of Acoustic Emission Characteristics under the Influence of Different Parameters

Figure 20 shows the proportion and number of cracks after the final failure of the coal body with different drilling depths, drilling diameters, and drilling angles. It can be seen from Figure 20 that the above three physical factors had little effect on the proportion of cracks after the final failure of coal. With the increase in drilling depths, drilling diameters, and drilling angles, the mixed fractures were kept at a low proportion (less than 10%), and the proportion of tensile fractures and shear fractures reached more than 90%, indicating that in the process of pressure relief of drilling, the failure forms were mainly tensile and shear failure. However, the drilling depths, drilling diameters, and drilling angles had a significant effect on the number of cracks after the final failure of the coal body. With the increase of drilling depths, the three kinds of fractures showed a trend of decreasing first, then increasing, and then decreasing in Figure 20a. When the drilling depth was 30 mm, the number of cracks was the lowest, which is consistent with the optimal critical value of the pressure relief effect with the drilling depth of 30 mm. With the increase of the diameter of the drilling, the three kinds of fractures showed a trend of decreasing slowly at first, then

decreasing rapidly, and finally remaining unchanged in Figure 20b. When the diameter of the drilling was 14 mm, the number of cracks was at a low level, which is consistent with the critical value of the pressure relief effect of the previous borehole diameters of 14 mm. With the increase of the drilling angles, the three fractures all showed a trend of decreasing rapidly first, then decreasing rapidly, and finally remaining unchanged in Figure 20c. When the drilling diameter was 25°, the the number of cracks was at a low level, which is consistent with the critical value of the pressure relief effect of the previous drilling angles of 25°.

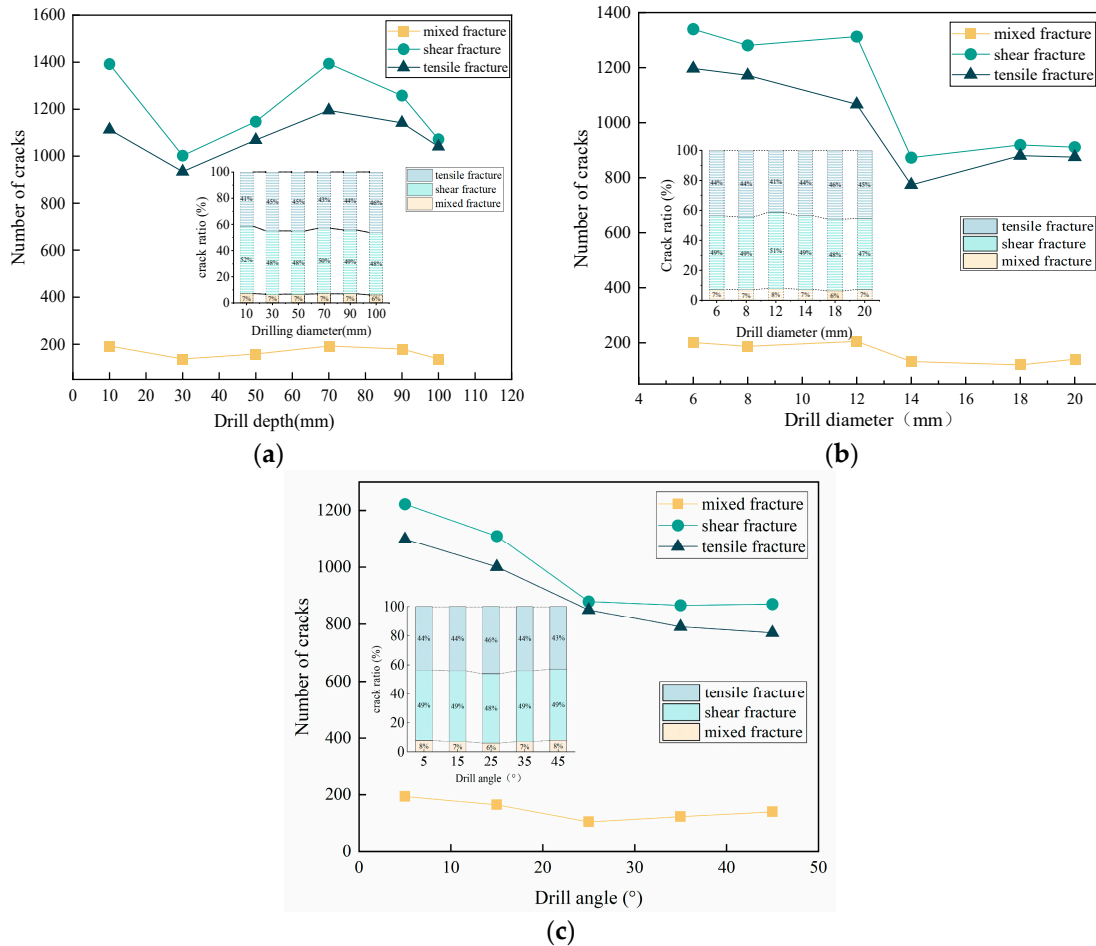


Figure 20. The proportion of cracks under the influence of different parameters. (a) Different drilling depth. (b) Different drilling diameter. (c) Different drilling angle.

From Figures 21–23, the moment tensor characteristics, AE characteristics, and b-value characteristics under different diameters, drilling depths, and drilling angles can be obtained. The specific analysis is as follows:

(1) Under different drilling diameters, the moment tensor amplitude of coal was mainly distributed in $-7.75 \sim -4.75$, and the peak value appeared in $-6.75 \sim -6.5$. Under different drilling depths, the moment tensor amplitude of coal was mainly distributed in $-7.5 \sim -5.0$, and the peak value appeared in $-6.75 \sim -6.5$. Under different drilling angles, the moment tensor amplitude of coal was mainly distributed in $-7.25 \sim -5.5$, and the peak value appeared in $-7.0 \sim -6.75$. Under different conditions, the relationship between the moment tensor size and the number of AE events obeyed the normal distribution.

(2) In the same amplitude range, the number of AE events was affected by the drilling diameters, drilling depths, and drilling angles. When the drilling diameter was 6~14 mm, the number of AE events showed a decreasing trend with the increase of the drilling diameter. When the drilling diameter was 14~20 mm, the number of AE events increased with the increase of aperture. When the drilling depth was 10~30 mm, the number

of AE events shows a decreasing trend with the increase of the drilling diameter. When the drilling diameter was 30~100 mm, the number of AE events increased first and then decreased with the increase of drilling diameter. When the drilling angle was 5~25°, the number of AE events decreased with the increase of the drilling angle. When the drilling angle was 25~45°, the number of AE events increased first and then decreased with the increase of the drilling angle.

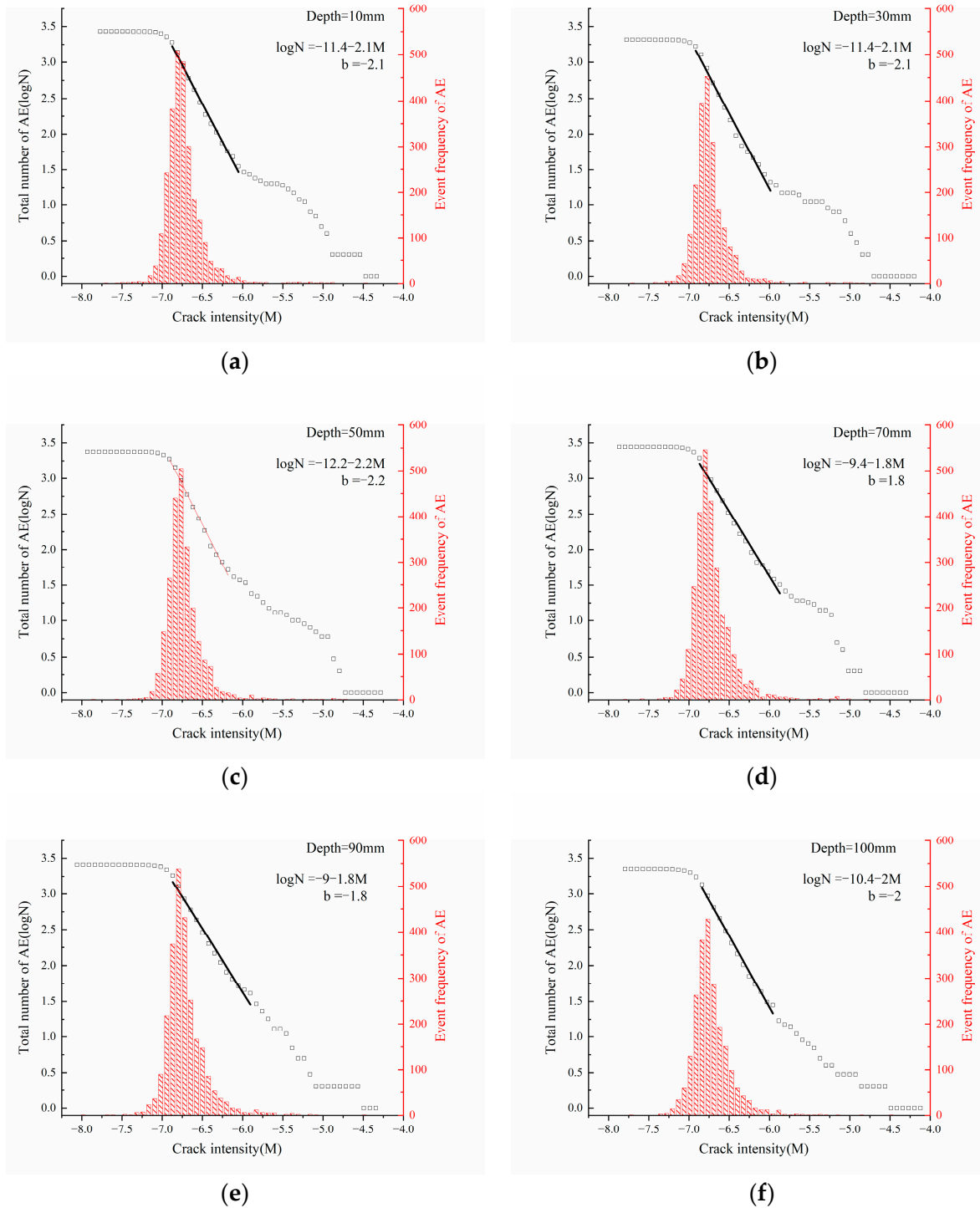


Figure 21. Distribution of moment tensor amplitude for different drilling depths. (a) 10 mm, (b) 30 mm, (c) 50 mm, (d) 70 mm, (e) 90 mm, (f) 100 mm.

(3) The changing trend of the b-value was closely related to the drilling diameters, drilling depths, and drilling angles. As shown in Figure 21, With the increase of drilling depths, the b-value increased first, then decreased, and finally increased again. With the increase of drilling diameters in Figure 22, the b-value generally showed a trend of increasing first, then decreasing, and finally stabilizing. With the increase of drilling angles in Figure 23, the b-value generally showed a trend of increasing first and then stabilizing.

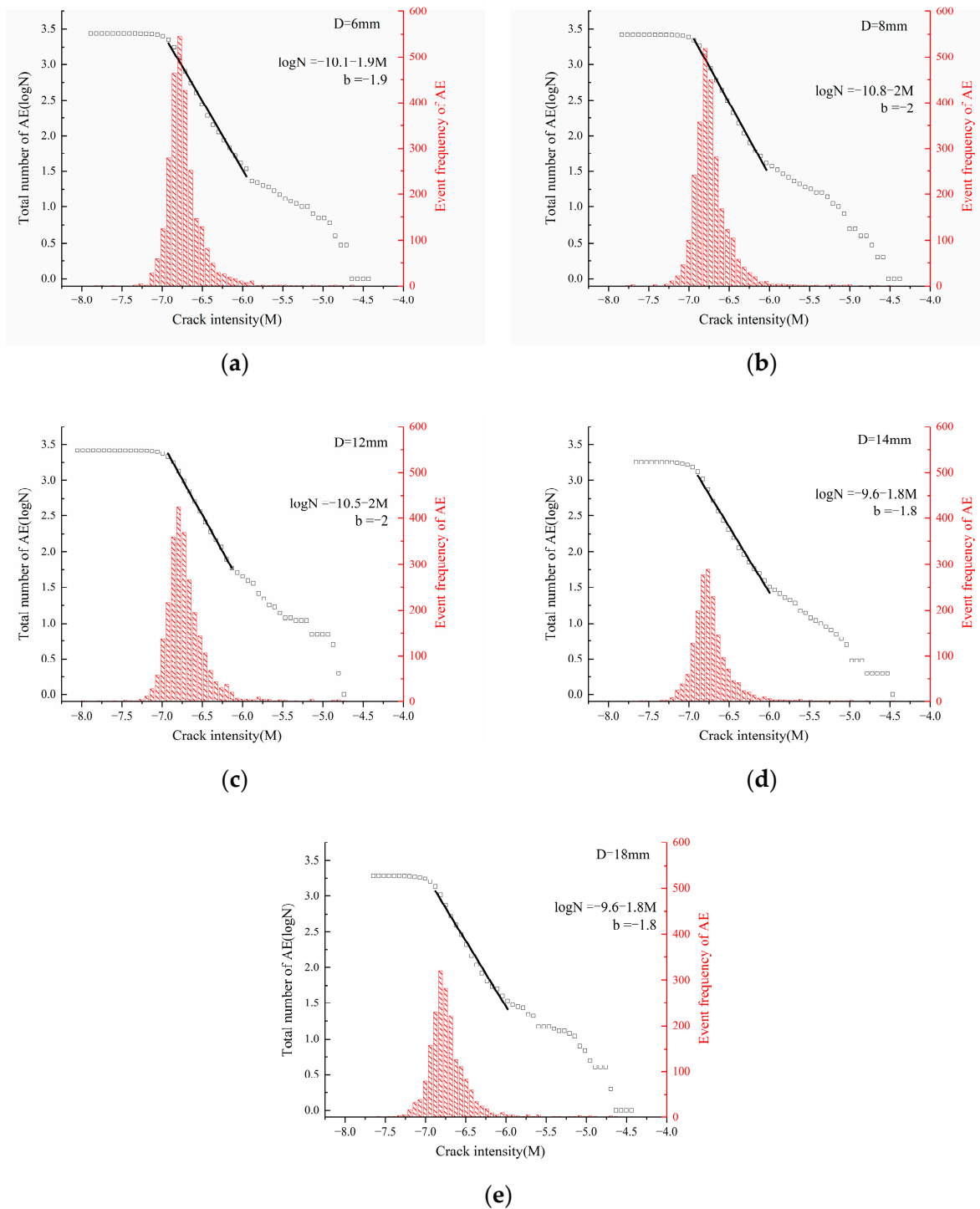


Figure 22. Distribution of moment tensor amplitude for different drilling diameters. (a) 6 mm, (b) 8 mm, (c) 12 mm, (d) 14 mm, (e) 18 mm.

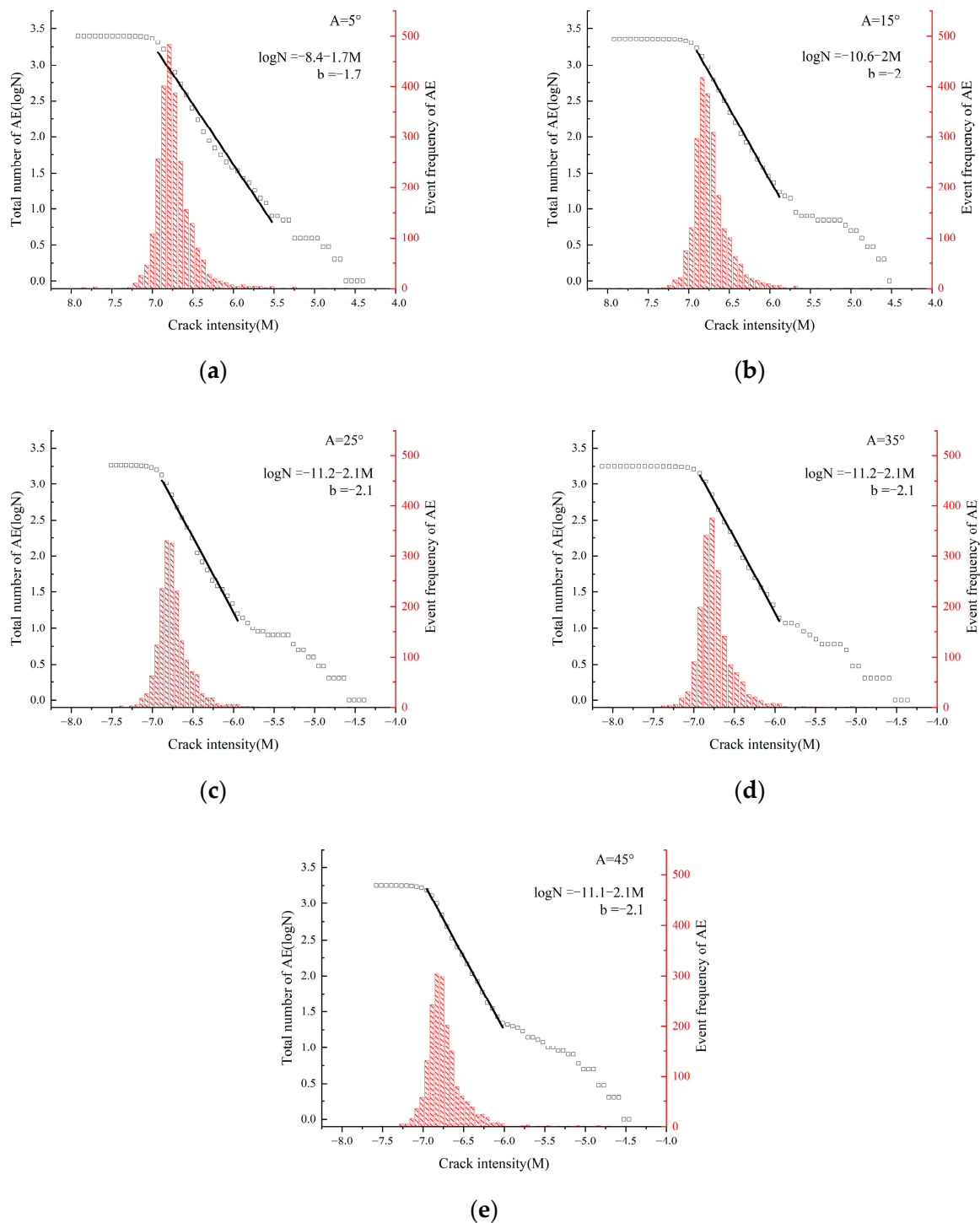


Figure 23. Distribution of moment tensor amplitude for different drilling angles. (a) 5° , (b) 15° , (c) 25° , (d) 35° , (e) 45° .

6. Conclusions

This paper is based on the basic principle of drilling pressure relief to prevent rock bursts, as well as considering the scale-independent properties of the damage localization mechanical behavior and the fracture process of rock-like material catastrophe. On the basis of the uniaxial compression mechanical behavior of coal samples at the laboratory scale, the PFC particle flow theory was applied to explore the changes in acoustic emission and the overall strength weakening effect during drilling pressure relief under different

physical influencing factors. The purpose was to clarify the effect of drilling pressure relief under various physical influencing factors, and to provide a regular understanding of the optimal parameter scheme for the construction of a single borehole. The main conclusions are as follows:

(1) With the increase of drilling depth, the peak strength of coal samples decreases rapidly first and then increases slowly, and then decreases slowly. With the increase of drilling diameter, the peak strength of coal samples decreases rapidly and then decreases slowly. With the increase of drilling angle, the peak strength of coal samples decreases first and then increases. Among them, the drilling depth of 30 mm, the drilling diameter of 14 mm, and the drilling angle of 25° are the critical thresholds when the above peak strength is low, indicating that when these values are taken, the drilling pressure relief effect is relatively good.

(2) When the coal sample is under the condition of a drilling depth of 30 mm, a drilling diameter of 14 mm, and a drilling angle of 25° , the location of the failure crack and the distribution of the force chain in the surrounding area are evacuated, and the color of the force chain is darker and the size of the force chain is smaller, which proves that this area has a better pressure relief effect, which is consistent with the above conclusions. The spatial distribution of cracks in coal samples is consistent with the spatial distribution of seismic sources. With the increase of hole depth, drilling diameter, and drilling angle, the cracks show the characteristics of changing from conjugate shear fractures to single inclined plane shear fractures, and the critical thresholds of transition are a drilling depth of 30 mm, a drilling diameter of 14 mm, and a drilling angle of 25° .

(3) Under various conditions, shear fractures and tensile fractures account for a very high proportion, indicating that these two fracture modes are the main types of microscopic fracture of coal samples, and the proportion of shear fractures is slightly higher than that of tensile fractures. When the drilling depth is 30 mm, the drilling diameter is 14 mm, and the drilling angle is 25° , the number of cracks is at a lower level.

(4) The moment tensor values of coal sample drilling are mainly distributed in the range of $-7.5\sim-5.0$, and the peak values mainly appear in the range of $-7.0\sim-6.5$. The relationship between the M value and N value is generally subject to normal distribution. When the drilling depth is 30 mm, the drilling diameter is 14 mm, and the drilling angle is 25° , the number of AE events is relatively low. With the increase of the hole diameter, the b value first increases and then decreases, and finally tends to be stable. With the increase of the drilling depth, the b-value first increases and then decreases, and finally increases again. With the increase of the drilling angle, the b-value first increases and then stabilizes. It shows that the events with small AE energy account for a large proportion when the drilling depth, drilling diameter, and drilling angle are small.

Author Contributions: Methodology, S.Z.; Software, S.Y.; Formal analysis, J.M. and J.L.; Investigation, J.M., J.L., S.Z., S.Y. and X.D.; Data curation, J.L., S.Y., X.D. and D.L.; Writing—original draft, J.M.; Writing—review & editing, J.M.; Visualization, J.L., X.D. and D.L.; Supervision, J.M., S.Z. and S.Y. All authors have read and agreed to the published version of the manuscript.

Funding: This research was funded by National Natural Science Foundation of China grant number 52274186.

Data Availability Statement: Data are contained within the article.

Conflicts of Interest: The authors declare no conflict of interest.

References

1. Zhao, T.B.; Guo, W.Y.; Tan, Y.L.; Yin, Y.C.; Cai, L.S.; Pan, J.F. Case Studies of Rock Bursts Under Complicated Geological Conditions During Multi-seam Mining at a Depth of 800 m. *Rock Mech. Rock Eng.* **2018**, *51*, 1539–1564. [[CrossRef](#)]
2. Zhou, F.B.; Xia, T.Q.; Wang, X.X.; Zhang, Y.F.; Sun, Y.N.; Liu, J.S. Recent developments in coal mine methane extraction and utilization in China: A review. *J. Nat. Gas Sci. Eng.* **2016**, *31*, 437–458. [[CrossRef](#)]
3. Gong, F.Q.; Yan, J.Y.; Li, X.B.; Luo, S. A peak-strength strain energy storage index for rock burst proneness of rock materials. *Int. J. Rock Mech. Min. Sci.* **2019**, *117*, 76–89. [[CrossRef](#)]

4. Yin, Y.C.; Zhou, H.J.; Zhang, Y.B.; Wang, C.; Deng, Y.H.; Chen, B.A. Anchorage weakening effect of coal roadway sidewall with different destressing borehole diameters. *Energy Sci. Eng.* **2023**, *11*, 1325–1335. [[CrossRef](#)]
5. Chen, M.; Zhang, Y.L.; Zang, C.W.; Zhang, G.C.; Li, Q.; Jiang, B.Z. Experimental Investigation on Pressure Relief Mechanism of Specimens with Prefabricated Reaming Boreholes. *Rock Mech. Rock Eng.* **2023**, *56*, 2949–2966. [[CrossRef](#)]
6. Lan, Y.W.; Zhang, Y.J.; Gao, H.M. Research on the Mechanism of Floor Heave of Roadway in Deep Mining. *Kuangye Yanjiu Yu Kaifa Min. Res. Dev.* **2005**, *25*, 34–36.
7. Ortlepp, W.; Stacey, T. Rockburst mechanisms in tunnels and shafts. *Tunn. Undergr. Space Technol.* **1994**, *9*, 59–65. [[CrossRef](#)]
8. Reyes, O.; Einstein, H. Failure mechanisms of fractured rock—a fracture coalescence model. In Proceedings of the 7th ISRM Congress, Aachen, Germany, 16–20 September 1991.
9. Pan, Y.; Zhao, G.M.; Meng, X.R. Elastic-plastic analysis of roadway surrounding rock under non-uniform stress field. *J. China Coal Soc.* **2011**, *36*, 53–57.
10. Wu, H.; Zhao, G.Y.; Liang, W.Z. Mechanical properties and fracture characteristics of pre-holed rocks subjected to uniaxial loading: A comparative analysis of five hole shapes. *Theor. Appl. Fract. Mech.* **2020**, *105*, 18. [[CrossRef](#)]
11. Liu, J.H.; Jiang, F.X.; Wang, N.G. *Roof Movement Disaster Control of Long Fully Mechanized Caving Face in Deep Topsoil*; Beijing Science Press: Beijing, China, 2013.
12. Zhang, H.; Li, T.; Ouyang, Z.H.; Liu, S.; Yi, H.Y. Research on Optimization of Coal Pressure Relief Borehole Parameters under High-Stress Conditions. *Geofluids* **2021**, *2021*, 13. [[CrossRef](#)]
13. Zhang, S.C.; Li, Y.Y.; Shen, B.T.; Sun, X.Z.; Gao, L.Q. Effective evaluation of pressure relief drilling for reducing rock bursts and its application in underground coal mines. *Int. J. Rock Mech. Min. Sci.* **2019**, *114*, 7–16. [[CrossRef](#)]
14. Li, Y.Y.; Guo, R.W.; Zhang, S.C.; Chen, B.; Yan, H.; Meng, W.; Zheng, D. Experimental Study on Pressure Relief Mechanism of Variable-Diameter Borehole and Energy Evolution Characteristics of the Surrounding Rock. *Energies* **2022**, *15*, 6596. [[CrossRef](#)]
15. Bahrehdar, M.; Lakirouhani, A. Effect of eccentricity on breakout propagation around noncircular boreholes. *Adv. Civ. Eng.* **2023**, *2023*, 6962648. [[CrossRef](#)]
16. Qin, Z.H. Study of Pressure Relief with Large Diameter Drilling Hole and Results Verified. *J. Min. Strat. Control* **2018**, *23*, 77–80.
17. Liu, H.G.; He, Y.N.; Xu, J.H.; Han, L.J. Numerical simulation and industrial test of boreholes destressing technology in deep coal tunnel. *J. China Coal Soc.* **2007**, *32*, 33–37.
18. Liang, S.W.; Zhang, L.; Ge, D.; Wang, Q. Study on Pressure Relief Effect and Rock Failure Characteristics with Different Borehole Diameters. *Shock Vib.* **2021**, *2021*, 10. [[CrossRef](#)]
19. Liu, H.G.; Xu, J.H. Numerical simulation and application of borehole pressure relief mechanism in coal roadway. *Coal Sci. Technol. Mag.* **2003**, *4*, 37–38.
20. Wen, Y.L.; Zhang, G.J.; Zhang, Z.Q. Numerical experiments of drilling pressure relief preventing roadway rock burst. In Proceedings of the 3rd International Conference on Civil Engineering, Architecture and Building Materials (CEABM 2013), Jinan, China, 24–26 May 2013; pp. 1583–1587.
21. Wang, T.X.; Cao, H.J.; Zhang, Z.Y. Numerical Simulation and Field Practice of Pressure-relief Borehole to Prevent Coal Burst in Deep-seated Coal Roadway. In Proceedings of the 2nd International Conference on Mine Hazards Prevention and Control, Qingdao, China, 15–17 October 2010; pp. 1583–1587.
22. Jia, C.Y.; Jiang, Y.J.; Zhang, X.P.; Wang, D.; Luan, H.J.; Wang, C.S. Laboratory and numerical experiments on pressure relief mechanism of large-diameter boreholes. *Chin. J. Geotech. Eng.* **2017**, *39*, 1115–1122.
23. Itasca. *PFC 6.0 Documentation, User's Guide*, Version 6.00.13; Itasca Consulting Group: Minneapolis, MN, USA, 2019.
24. Potyondy, D.O. Simulating stress corrosion with a bonded-particle model for rock—ScienceDirect. *Int. J. Rock Mech. Min. Sci.* **2007**, *44*, 677–691. [[CrossRef](#)]
25. Potyondy, D.O.; Cundall, P. A bonded-particle model for rock. *Int. J. Rock Mech. Min. Sci.* **2004**, *41*, 1329–1364. [[CrossRef](#)]
26. Hazzard, J.F.; Young, R.P. Moment tensors and micromechanical models. *Tectonophysics* **2002**, *356*, 181–197. [[CrossRef](#)]
27. Hazzard, J.F.; Young, R.P. Dynamic modelling of induced seismicity. *Int. J. Rock Mech. Min. Sci.* **2004**, *41*, 1365–1376. [[CrossRef](#)]
28. Silver, P.G.; Jordan, T.H. Optimal estimation of scalar seismic moment. *Geophys. J. Int.* **2010**, *70*, 755–787. [[CrossRef](#)]
29. Hanks, T.C.; Kanamori, H. A moment magnitude scale. *J. Geophys. Res.* **1979**, *84*, 2348. [[CrossRef](#)]
30. Wang, K.; Zhang, X.; Du, F.; Li, K.N.; Sun, J.Z.; Wang, Y.Q. Numerical study on damage response and failure mechanism of gas-containing coal-rock combination under confining pressure effect. *Fuel* **2023**, *349*, 17. [[CrossRef](#)]
31. Yu, W.; Yu, L.; Yao, D. A bonded-particle model for rock. *J. Chengdu Univ. Technol. Sci. Technol. Ed.* **2021**, *48*, 714–722.

Disclaimer/Publisher's Note: The statements, opinions and data contained in all publications are solely those of the individual author(s) and contributor(s) and not of MDPI and/or the editor(s). MDPI and/or the editor(s) disclaim responsibility for any injury to people or property resulting from any ideas, methods, instructions or products referred to in the content.